Research Article | Vol. 26, No. 23 | 12 Nov 2018 | OPTICS EXPRESS 30952

Optics EXPRESS

Structural coloration with hourglass-shaped vertical silicon nanopillar arrays

Brian M. Gawlik,[1,*] Gabriel Cossio,[2] Hoyeong Kwon,[2] Zulema Jurado,[1,6] Briana Palacios,[1,6] Shrawan Singhal,[1] Andrea Alù,[2,3,4,5] Edward T. Yu,[1,2] and S. V. Sreenivasan[1]

[1]*NASCENT Center, The University of Texas at Austin, Austin, Texas 78758, USA*
[2]*Department of Electrical and Computer Engineering, The University of Texas at Austin, Austin, Texas 78758, USA*
[3]*Photonics Initiative, Advanced Science Research Center, City University of New York, New York, NY 10031, USA*
[4]*Physics Program, Graduate Center, City University of New York, New York, NY 10016, USA*
[5]*Department of Electrical Engineering, City College of The City University of New York, NY 10031, USA*
[6]*These authors contributed equally*
[*]*brian.gawlik@utexas.edu*

Abstract: We demonstrate that arrays of hourglass-shaped nanopillars patterned into crystalline silicon substrates exhibit vibrant, highly controllable reflective structural coloration. Unlike structures with uniform sidewall profiles, the hourglass profile defines two separate regions on the pillar: a head and a body. The head acts as a suspended Mie resonator and is responsible for resonant reflectance, while the body acts to suppress broadband reflections from the surface. The combination of these effects gives rise to vibrant colors. The size of the nanopillars can be tuned to provide a variety of additive colors, including the RGB primaries. Experimental results are shown for nanopillar arrays fabricated using nanoimprint lithography and plasma etching. A finite difference time domain (FDTD) model is validated against these results and is used to elucidate the electromagnetic response of the nanopillars. Furthermore, a COMSOL model is used to investigate the angle dependence of the reflectance. In view of display applications, a genetic algorithm is used to optimize the nanopillar geometries for RGB color reflective pixels, showing that nearly all of the sRGB color space and most of the Adobe RGB color space can be covered with this technique.

1. Introduction

Among many exciting phenomena exhibited by nanostructured materials, structural coloration is one of the most fascinating. Unlike dyes and pigments, whose color depends on the absorptive properties of materials, structural colors leverage optical effects that rely primarily on geometric structure and are commonly found in the natural world, such as in the opal stone [1], the wings of the morpho butterfly [2–5], and the skin of panther chameleons [6].

Structural colors can also be man-made [5,7–10] and have unique qualities that may offer advantages over dyes and pigments for use in prints and displays. Because they are typically made from inorganic materials, they generally have superb chemical and mechanical stability which could create immunity to fading and bleaching. These materials also lend themselves better to recyclability compared to the organics used in pigments. Finally, the scalability of structural colors to extremely small length scales can be utilized to create color pixels as small as the diffraction limit of light [11], allowing for ultra-high resolution and/or micro-displays and prints.

Until recently, focus had been placed on plasmonic nanostructures for the creation of structural colors [9,10,12]. Some impressive demonstrations of high-spatial resolution, full

#341848 https://doi.org/10.1364/OE.26.030952
Journal © 2018 Received 15 Aug 2018; revised 30 Sep 2018; accepted 7 Oct 2018; published 9 Nov 2018

Optics EXPRESS

color printing based on plasmonics have been reported, including a replica of Monet's painting *Impression, Sunrise* at ~300 um in size [13] and the Lena Image at 100,000 DPI [11]. As impressive as these demonstrations have been, plasmonic colors have ultimately failed to compete with traditional pigments: the colors they have produced are not as saturated as required, due to the high losses in these materials at visible wavelengths, and to other material-specific issues, such as the inability of gold to support strong resonances at blue wavelengths, or the vulnerability of silver to chemical degradation in air [14].

Because of these shortcomings, the research focus has recently shifted towards structural colors based on dielectric materials. Dielectrics can create color through a variety of phenomena, including grating diffraction, guided mode resonance (GMR) in horizontal 1D subwavelength gratings [15–17] and vertical nanowire arrays [18–20], interferometric cavities [21–23], optical bandgap properties of photonic crystals [24–26], and resonant Mie scattering [8,27–31]. With the application of prints and reflective displays in mind, Mie metasurfaces have produced the most compelling results, due to their sub-wavelength size which prevents diffraction and due to their relative insensitivity to polarization and viewing angle.

Multiple authors have demonstrated angle-independent, high-saturation, wide-gamut colors based on all-dielectric Mie metasurfaces [32–45]. These embodiments have been based on variations of a common architecture, consisting of a 2D array of high-index (i.e. Si, SiGe alloys, TiO_2), low-aspect ratio nanostructures on a low-index substrate (i.e. glass), which provides enough contrast to sustain the Mie resonances and does not create unwanted reflections at the substrate/air interface. The need for a low-index substrate implies that the same structural coloration cannot be achieved by simply patterning the surface of a high-index substrate – such as crystalline Si (c-Si) – with the same nanostructures, which may be desirable for integration with Si electronics, such as for reflective display devices. One implementation of low-aspect ratio Mie structures has overcome the issue of Fresnel reflections from a Si substrate by placing amorphous Si resonators on a Si substrate coated with an anti-reflective Si_3N_4 layer [44]. This acts to mimic floating the resonators in free-space. In our work, we achieve a similar floating resonator function but do so by suspending the resonator on a high-aspect ratio tapered body. This is similar to a structure explored by previous work in which an annealing process naturally transformed cylindrical Si structures into pedestalled spheroids [45]. However, the fabrication process in our work enables more precise control over the shape and dimensions of the resonator volume.

In this paper, we demonstrate the creation of a wide range of structural colors via Mie metasurfaces fabricated directly from c-Si substrates by embracing the natural tendency of plasma etching to create hourglass-shaped structures. We demonstrate this hourglass-like structure experimentally, explore its optical behavior, and use a genetic algorithm to optimize the structures to create the three RGB primary colors in both the sRGB and Adobe RGB color spaces. It should be noted that in this paper, we only explore the structural color itself and not a means for modulating its intensity, which is necessary for applications such as display devices. However, solutions have been explored in the literature to modulate light intensity and color for a variety of different types of structural color filters [24,46–48].

2. Methods

2.1 Device fabrication

Mie metasurfaces were fabricated from 4" double-side polished single-crystalline Si wafers as illustrated in Fig. 1. First, 100 nm of SiO_2 was thermally grown on the wafers for use as an etch hardmask. Then, the samples were imprinted using an imprint template containing square arrays of pillars with 130 nm diameter and 200 nm pitch. The template has the arrays defined in 1x1 mm squares separated by ~100 um from each other and arranged in a ring on the wafer with a small area in the middle which can be seen in the full wafer photographs in Fig. 11 in Appendix D. The samples underwent a 25 s RIE etch on a Trion etch system – normally referred to as a "descum" etch – to remove the residual layer thickness (RLT) that naturally

Optics EXPRESS

forms between imprinted features. Pressure was 15 mT. Gases were 70 sccm Ar and 2 sccm O2. RIE power was 65 W. Then a 550 s RIE etch on the same Trion system was used to transfer the imprinted pattern into the SiO_2 hardmask. Pressure was 110 mT. Gases were 50 sccm Ar, 15 sccm CHF3, and 5 sccm CF4. RIE power was 125 W. Another 120 s plasma etch was done on an STS etch system which was used to transfer the pattern into the Si substrate. Pressure was 30 mT. Gases were 80 sccm Hbr and 12 sccm Cl_2. Coil power was 700 W and platen power was 150 W. The nominal diameter of the template (~130 nm) produced the green color. In order to get blue and orange colors, we changed the size of the mask features before the Si etch. This was done in two ways: To make them smaller the descum was run longer than normal such that the resist pillar diameters would shrink in size diametrically, and to make them larger, atomic layer deposition (ALD) of SiO_2 was done on a FIJI ALD system to increase the diameter of the SiO_2 mask features. 125 cycles of ALD were done with alternating tris(dimethylamino)silane (TDMAS) and O_2 gases at 110°C which deposited approximately 10 nm of SiO_2. A short SiO_2 etch was done on the Trion (same parameters as above), to break through the SiO_2 layer deposited on the surface in between the features.

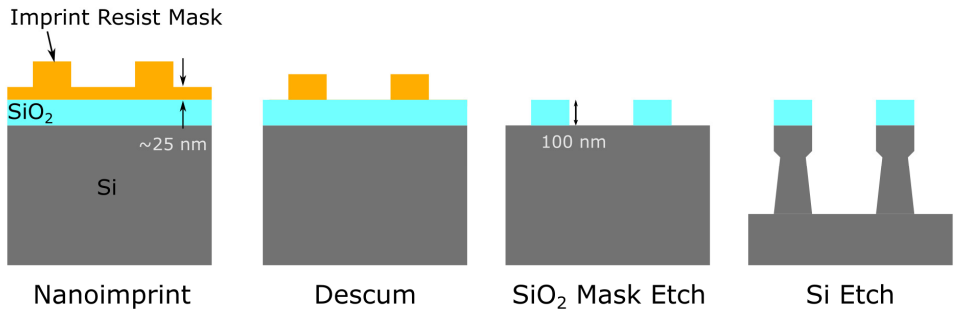

Fig. 1. Schematic showing the nanopillar fabrication process.

2.2 Simulations

Lumerical FDTD was used for the simulations presented in the experimental results section and the optimization section. The pillar was assembled bottom-to-top with a series of thin disks of varying diameters conforming to the hourglass profile of the pillar. Linear transitions in diameters were assumed. In the simulation region, periodic boundary conditions were used in the x- and y-directions, and PML boundary conditions were used at the z-boundaries on the bottom and top. The Si and SiO_2 materials were taken from the default library. A plane wave ranging from 360 to 830 nm was normally incident from above the pillar, and a monitor was placed above the pillar for the reflectance calculation.

COMSOL Multiphysics was used for the simulations performed as functions of angle of incidence. An angular range of 0-89° in steps of 1° was studied. Boundary conditions and monitors were set up identically to the Lumerical simulations. The pillar shape was defined using truncated conics. A plane wave was illuminated from the top of the structure from 360 to 830 nm in steps of 5 nm.

2.3 Optical characterization

A custom imaging spectrophotometer was used for the experimental reflectance measurements at normal incidence. Unpolarized collimated light from a Xenon arc lamp was spectrally resolved by a monochromator and was then made incident on the sample. The normal incidence reflectance was imaged by a camera. Measurements were done from 400 to 700 nm in steps of 5 nm. This system has a spatial resolution of ~5 um, so points in the sample very near to the exact location of the cross-section SEM measurements could be characterized. A high-quality aluminum mirror was used as a reference standard.

Optics EXPRESS

Optical reflectance measurements at different angle of incidence (AOI) were performed using a traditional spectrophotometer. In this system, unpolarized collimated light from a halogen lamp was spectrally resolved by a monochromator and was then incident on the sample at variable AOI. The specular reflection was collected by a detector with AC lock in detection. Devices were mounted on a rotating stage, allowing measurements to be performed at angles from 15° to 65°. Measurements were done from 400 to 700 nm in steps of 5 nm. The unaltered beam from the light source was measured as the reference.

2.4 Genetic algorithm optimization

A genetic algorithm (GA) from the MATLAB Global Optimization Toolbox was used to optimize the geometry of the nanopillars to produce RGB primary colors from two different color spaces, sRGB and Adobe RGB. In each case, the GA fed different combinations of 7 parameters (with the pitch being fixed) describing the nanopillar geometry into an objective function whose value was to be minimized. The objective function would first run an FDTD simulation of a nanopillar lattice described by the current set of geometric parameters using the wavelength range of 360-830 nm and then would use the resulting reflectance spectrum returned by the simulation along with the CIE 1931 color matching functions to calculate the x and y chromaticity coordinates of the color corresponding to the reflectance. Then, the objective function calculated the straight-line distance in xy chromaticity space (CIE 1931) between the chromaticity of the simulated structural color and a target chromaticity – either red, green, or blue as defined by the sRGB and Adobe RGB primary coordinates (listed below). The GA was first run with the FDTD set to a low mesh accuracy to allow for quick individual simulations. Then once the GA was finished, the best set of parameters was used to run another FDTD simulation at a high mesh accuracy to insure the accuracy of the resulting reflectance. The result at the high accuracy mesh was reported in the main text. The following linear constraints were imposed upon the optimization to reflect the general shape and geometric constraints of the pillars (i.e. diameters must be less than the pitch, neck diameter is less than head diameter, etc.): $A \leq P$, $B \leq C-10$, $B \leq D-10$, $B \geq 10$, $C \leq A$, $D \leq A$, $E \leq F-10$, $E \geq 0.5*H$, $F \leq H-10$. The use of 10 nm in certain cases (i.e. $B \leq C-10$) was used to make sure that certain parameters were not chosen to be too close to one another or unrealistically small. The color space primaries were as follows: sRGB (x,y): R(0.640, 0.330), G(0.300, 0.600), B(0.150, 0.060). Adobe RGB (x,y): R(0.640, 0.330), G(0.210, 0.710), B(0.150, 0.060).

3. Results and discussion

3.1 Experimental demonstration of structural color

Figure 2 shows three experimental hourglass structures. Arrays of each structure are shown in the scanning electron microscope (SEM) images in Fig. 2(a) and the colors they create (as observed with an optical microscope) are shown in Fig. 2(b) (sample correspondence is by row). We have used this structure to create blue, green, and orange colors. Each color is the result of a prominent peak in the visible reflectance spectrum as shown in Fig. 2(c).

Optics EXPRESS

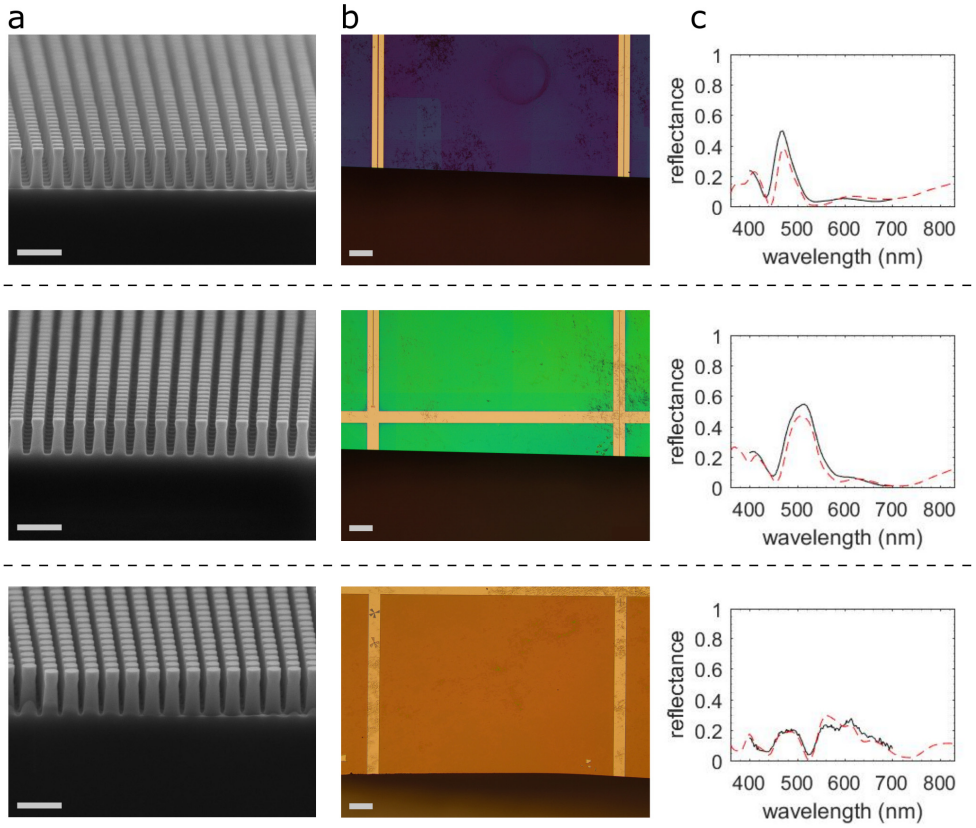

Fig. 2. (a) Tilted cross-sectional SEM (Scanning Electron Microscopy) images (scale bar 400 nm), (b) 5X microscope images of samples (scale bar 100 µm), and (c) Experimental and simulated reflectance spectra (solid black and red dashed lines, respectively) of the corresponding samples (by row). In (b), the large squares contain the nanopillar arrays, and the "streets" in between the squares contain bare Si and occasionally some alignment structures. The bare Si appears yellow in the images due to the yellow hue of the source lamp in the microscope. Geometric parameters for the simulations in (c) are taken from cross-sectional SEMs as detailed in Fig. 3. A thin oxide layer is added to the simulation to account for surface etch roughness and oxidation (5 nm for blue, 3 nm for green, 0 nm for red). In (c) the simulation wavelength range is from 360 to 830 nm, but the experimental measurement was limited to 400-700 nm.

As we will show, this strong coloration arises from resonant Mie scattering, primarily from the heads of the pillars. The color can be tuned by changing the size of the head of the pillars, and in general, smaller heads produce resonances at shorter wavelengths. In each case, the pillar maintains the same general hourglass profile, which is the essence of this structure. The neck of the hourglass geometrically isolates the head of the pillar from its body, which causes the head to respond to an impinging wave similarly to a dielectric particle suspended in free space.

The structures were fabricated using nanoimprint lithography and plasma etching. The plasma etch naturally created a "necked" hourglass-like structure, due to a combination of isotropic chemical etching and off-normal ion-bombardment. By adjusting the etch conditions and making use of atomic layer deposition (ALD), the features could either be shrunk or enlarged to create different colors, and all the arrays shown could be fabricated using a single nanoimprint template (see Methods). The template had a pitch of 200 nm, which was close to optimal for the blue and green colors but was too small to achieve a strong red color. This explains the orange color of the array with the largest pillars. The reason for this is that in

Optics EXPRESS

order to support resonances at larger wavelengths, the diameter of the pillars becomes larger, thus the spacing between the pillars decreases, causing the confinement of the Mie resonances in the pillars' heads to decrease. Simultaneously, the proximity of the pillars decreases the necking in the etch, and the heads cannot be as well defined. As we will show in the optimization section towards the end of the paper, it is possible to create very vibrant reds using a pattern with a larger pitch.

3.2 Numerical simulations of Mie resonant behavior

To provide deeper physical understanding of the resonant phenomenon supporting our structural colors, we performed numerical simulations using Lumerical finite difference time domain (FDTD) and COMSOL Multiphysics. The FDTD model was used to simulate normal incidence illumination. Our model consists of 8 different geometric parameters, illustrated in Fig. 3(a). Parameters (A-H) were measured at specific points on the samples using cross-section SEM while the pitch was assumed to be the nominal pitch of the nanoimprint template (200 nm). These measurements are tabulated in Fig. 3(b).

a

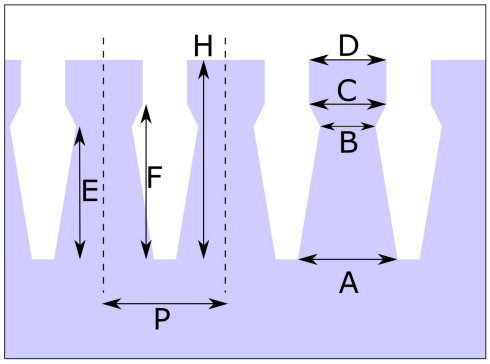

b

	A	B	C	D	E	F	H	P
Blue	135	83	102	104	283	335	383	200
Green	146	94	121	116	246	306	357	200
Orange	169	120	135	132	313	362	442	200

Fig. 3. (a) Schematic showing the structural parameters of the nanopillars and their corresponding labels. (b) SEM measurements (in nm) of the structural parameters for the three experimental structures shown in Fig. 2.

We also include a low-index layer on the outside of the pillars, which we attribute to surface roughness, native oxide, or a combination of both. Such a low-index layer would contribute to the thickness of the pillars as measured with the SEM resulting in an actual Si thickness which is slightly smaller than what is measured by SEM. Including a low-index layer in the form of native oxide to the simulations accounts for the presence of this layer, and its thickness can be tuned to produce a good match to the experimental reflectance. Interestingly, the thickness of this low-index layer required to produce good agreement with our measurements decreased as the diameter of the pillars increased (5 nm for blue, 3 nm for green, and less than the 1 nm simulation mesh size for red). We believe this effect is due to the thickness of the low-index layer being dependent on the size of the pillars, as pillars with smaller diameters require significantly more etch-removal of material and acquire more surface roughness during the etch. As a result, this can lead to deeper surface oxidation. The simulated reflectance with the adjusted low-index layer is overlaid with the experimental reflectance in Fig. 2(c) and shows good agreement.

Optics EXPRESS

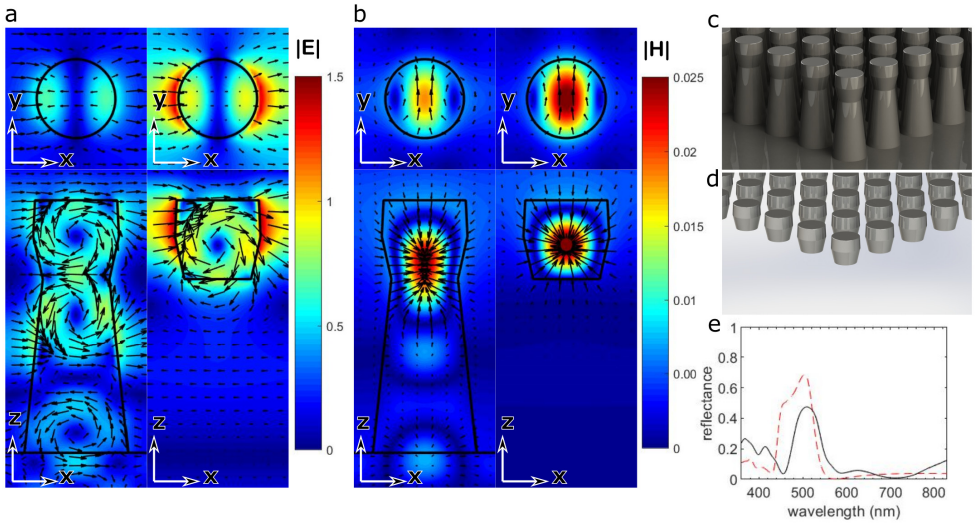

Fig. 4. (a) Electric field plots for the experimental green nanopillar array (left) and the corresponding floating head array (right). (b) Magnetic field plots for the nanopillar array (left) and floating head array (right). Background color plots are absolute value of the field and arrows are field vectors. (c) 3D model of the hourglass-shaped nanopillar array. (d) 3D model of the floating head array. (e) Reflectance of the two different structures (solid black is the nanopillar array and dashed red is the floating head array).

The FDTD model was used to study the electromagnetic field distributions and their relationship to the coloration. A simulation of the nanopillar array was run based on the pillar dimensions from the green experimental sample. Also, a simulation of an array of the heads of the nanopillars floating in free space, as illustrated in Fig. 4(d), was performed to demonstrate that this structure exhibits similar behavior to the nanopillar array. In the simulations, a plane wave impinges at normal incidence from above the array, and the resulting electric and magnetic field distributions at the wavelength of peak reflectance (520 nm for the pillars, 507 nm for the floating heads) are shown in Fig. 4(a) and 4(b) respectively. The field profiles of the pillars (left side of Fig. 4(a) and 4(b)) show that a magnetic dipole (MD) resonance is induced and localized in the head of the nanopillar. The right panels of Fig. 4(a) and 4(b) show that the floating head array supports a similar, but much better confined, MD resonance. Figure 4(e) shows that the corresponding reflectance spectra of the two structures are also quite similar. This comparison reveals that the primary role of the hourglass profile is to geometrically isolate the head of the pillar in air above the substrate, such that it functions as if it is floating. It is important for the neck to be narrow, so that there is better spatial isolation of the head and thus greater confinement of the MD mode. If the neck diameter is not narrow, electromagnetic energy “leaks” out of the head into the body, leading to decreased scattering efficiency. As we show in Fig. 7 in Appendix A, when the neck diameter is small, the geometric isolation becomes excellent and the optical behavior of the nanopillar arrays become almost identical to the case of the floating head. In addition to the resonance effect, the structural coloration is also aided by the subwavelength tapering of the body of the pillar, which enables index grading between the low index medium and the high index substrate. This suppresses broadband Fresnel reflections at the substrate/air interface, similar to moth-eye antireflection structures [49–51].

3.3 Dependence of color on angle of incidence

Since the resonance is mostly determined by the individual resonance of the single pillar head, and not by lattice phenomena, the color of the nanopillar array is not significantly affected by the angle of incidence (AOI) of the illumination. To the eye, the color of the green

Optics EXPRESS

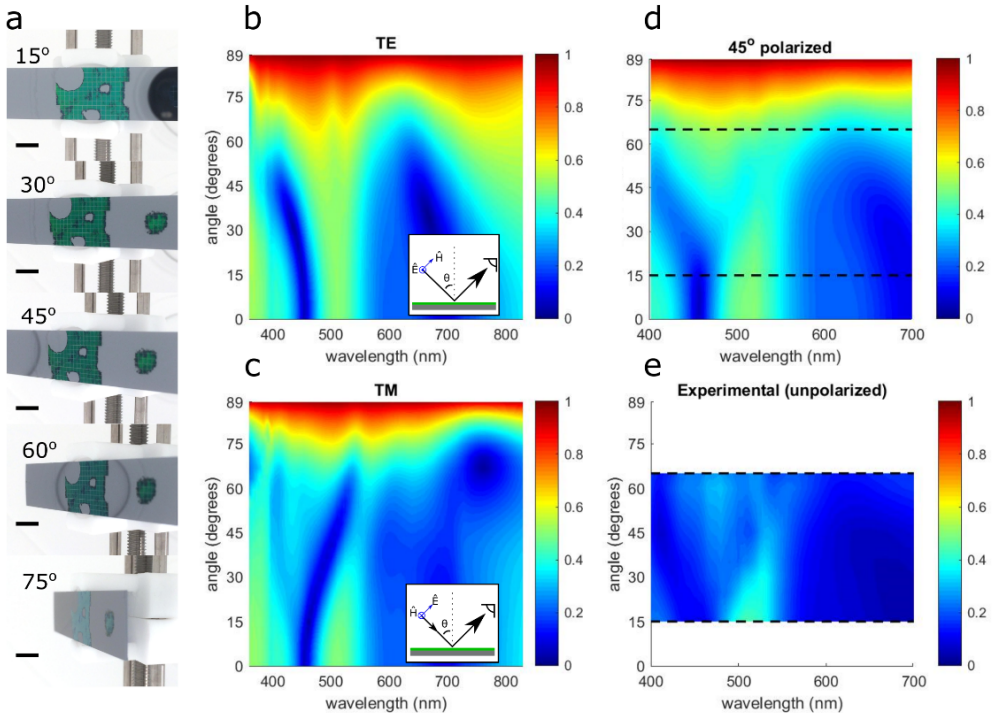

Fig. 5. (a) Photographs of the green sample at various angles taken inside an integrating sphere illuminated with white light (scale bar = 5 mm). Circular spots on the samples are areas of missing pattern caused by particles during imprinting. In order to correct for different exposure times and white points, each photo was adjusted to have the same RGB values at the same pixel corresponding to a point on the inner wall of the integrating sphere which was visible in each photograph. (b) Simulated angle-dependence of the nanopillar structure reflectance for TE polarized illumination. (c) Simulated angle-dependence of the nanopillar structure reflectance for TM polarized illumination. (d) Simulated angle-dependence of the nanopillar structure reflectance for 45° polarized illumination shown from 400 to 700 nm to match with experimental results. (e) Experimental angle-dependent reflectance of the nanopillar structure (unpolarized illumination). The range of angles corresponding to the unpolarized experimental measurement (15° to 65°) is shown bounded by the dotted black lines in (d) and (e). Experimental measurements were taken at 15°, 25 °, 30 °, 35 °, 45 °, 60 °, 65 ° and the plot was smoothed using interpolation.

experimental sample does not change significantly until >60° as shown in Fig. 5(a). To explore this angular independence, a COMSOL simulation is performed based on the green sample parameters from the experimental section. In this simulation, the AOI of the illumination is swept from 0° to 89° in steps of 1°. The simulations are performed with both TE and TM polarization and also for the 45° polarized case. Figure 5(b) and 5(c) show the reflectance profiles for the TE and TM modes. For the TE mode, the MD resonance is sustained at the same wavelength as the AOI increases, but the reflectance peak broadens due to another resonance arising in the entire pillar at shorter wavelengths. For the TM mode, the resonance moves to longer wavelengths as the AOI increases, and its intensity decreases significantly between 30° and 60°. A Brewster effect is responsible for this decrease. However, broadband Brewster transmission is not achieved as with slit metasurfaces [52], because of the contribution from the Mie resonance, which is sustained over this range of AOI. Electric and magnetic field profiles are provided in Figs. 8 and 9 in Appendix B which document these changes in the resonance. Next, Fig. 5(d) shows a simulation performed with 45° polarized illumination to compare to experimental measurements of unpolarized specular reflectance at different AOIs taken with a spectrophotometer as shown in Fig. 5(e). There is a

Optics EXPRESS

good agreement between the simulation and the unpolarized experimental measurement, although the experimental measurement apparatus was limited to measurements from 15 to 65° and 400-700 nm. The 45° polarized simulation result shows that at angles larger ~75° a much broader reflectance signature takes over, which is marked by many less prominent peaks across the visible spectrum and approaches broadband unity at parallel illumination.

3.4 Genetic algorithm optimization

The dimensions of the hourglass profile can be further optimized to produce more saturated colors. In view of display applications, we have run an optimization to determine ideal nanopillar geometries for achieving each of the three RGB primary colors of two common color spaces, sRGB and Adobe RGB. We have chosen to optimize for each color independently to demonstrate the full range of color possibilities.

Because of the relatively large number of individual parameters describing the shape of each nanopillar, taking a brute force approach and simulating results for the entire parameter space was not possible, and for this reason, a genetic algorithm (GA) search optimization was used. The two color spaces share common R and B coordinates, whereas the G points differ. So in total, four separate GA's were run. The GA ran our FDTD model with different combinations of the parameters A, B, C, D, E, F, and H, used the reflectance spectrum to compute its color in CIE chromaticity space, and optimized the matching of the colors to the coordinates of the primary colors specified by both color spaces (see Methods). To simplify the optimization, the pitch parameter P was fixed at 200 nm (based on the imprint template pitch) for the blue and green optimizations and set to 300 nm for the red optimization. Because the effect is a localized resonance, the pitch does not play a significant role in the color's hue but must be neither so small as to diminish the presence of the localized resonance nor so large as to allow Fresnel reflection to become the dominant scattering method. The results of the GA optimizations are shown in Fig. 6, and exact geometric parameter values of the results are listed in Fig. 6(d). Our optimization results show that it is feasible to produce very good RGB colors covering nearly all of the sRGB color space and most of the larger Adobe RGB color space as well. The primary reason why these optimized structures perform better than the experimental results is that the neck diameter (parameter B) is significantly smaller in the optimized pillars. The optimized neck diameters range from 35 to 64% of the average head diameter ((C + D)/2). In contrast, the necks on the experimental structures range from 81 to 90% with the highest percentage corresponding to the orange sample, which had the least vibrant color. The pillars clearly benefit from having a thin neck diameter, namely for two reasons: 1. The thin neck more effectively defines the head such that it better confines the MD resonance and 2. The thin neck produces more tapering along the length of the body, which helps grade the refractive index change at the substrate. Figure 7 in Appendix A shows the normal incidence reflectance and the field plots for the optimized Adobe RGB green result side-by-side with the corresponding floating head structure just as we showed in Fig. 4 for the experimental structures. The two sets of results are nearly identical, demonstrating that narrowing the neck creates a condition very similar to the floating head.

Optics EXPRESS

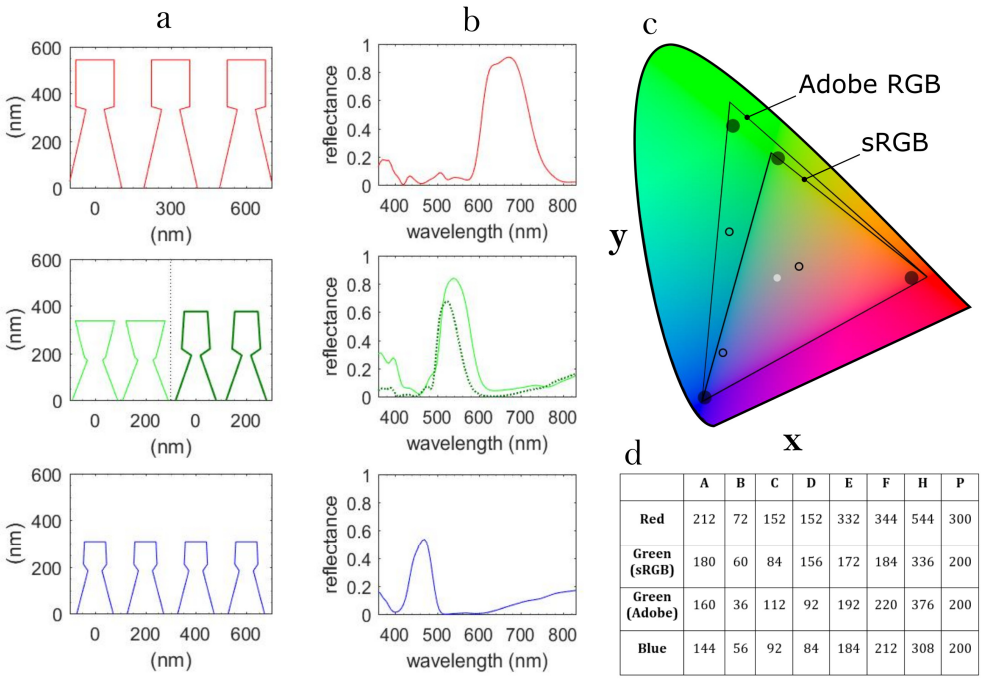

	A	B	C	D	E	F	H	P
Red	212	72	152	152	332	344	544	300
Green (sRGB)	180	60	84	156	172	184	336	200
Green (Adobe)	160	36	112	92	192	220	376	200
Blue	144	56	92	84	184	212	308	200

Fig. 6. Results of the genetic algorithm optimization. (a) Plots showing the optimized geometries for the pillars corresponding to red, green, and blue (top to bottom). There are two results for green: one for sRGB (left) and one for Adobe RGB (right). (b) Simulated reflectance corresponding (by row) to the optimized pillar geometries. For the green result, the Adobe RGB reflectance curve is shown by the darker, dotted green line. (c) CIE chromaticity plot with sRGB and Adobe RGB color spaces outlined by the black triangles, the D65 white point shown by the filled white circle in the middle, the three experimental results shown by the black empty circles, and the four optimization results shown by the filled black circles. (d) Table of the optimized parameter values (in nm).

The GA had more difficulty optimizing for the Adobe RGB green primary, because the color is much more saturated. The two green results are shown in the split middle panel of Fig. 6(a) (left side sRGB, right side Adobe RGB). The reason why the Adobe RGB pillars produce a greener hue is related to the more tapered body and the slight taper of the head. The slanted head would reduce broadband reflections from the interface between the top of the head and air, while the more tapered body would reduce broadband reflections from the substrate. In general, the reflectance of non-green wavelengths is clearly reduced in the Adobe RGB green case, producing a purer color, despite the peak reflectance being smaller. The difference between the sRGB green and the Adobe RGB green highlights just how sensitive these structures are to small variations in nanoscale geometry. This optical sensitivity could be exploited for metrology in a manufacturing setting to detect subtle nanoscale variations in geometry away from the target values. Such geometric variations could be obtained exactly using spectroscopic scatterometry, and this information could be used to pinpoint unique problems in specific fabrication steps such as under/over-etching, center-to-edge wafer variations, etc.

Through these optimizations, we show the potential of the hourglass pillar structure to create a broad range of individual colors. However in an RGB display device, the structures would need to be fabricated adjacent to one another in a subpixel mosaic pattern. It is of course possible to lithographically define different diameters and pitches for each subpixel region. It is also possible to use photolithographic techniques to etch each subpixel region separately by blanket masking two of the three subpixels at a time, thus creating the freedom

Optics EXPRESS

to optimize each etch process separately to achieve the desired shapes. If this is not an option, the option of etching all three subpixels simultaneously is also tenable. In Appendix C, we show one such demonstration where the red, green, and blue pillars are constrained to have the same height, along with the same head geometry and pitch as obtained from the GA results. Even with the height constraint, it is still possible to span nearly all of both the Adobe RGB and sRGB color spaces. The actual geometric constraints of such an etch are unknowable, but further optimizations could be done which constrain the pillars in each subpixel as necessary.

Although the RGB colors in this demonstration are discussed within the context of RGB display applications, the nanopillar arrays can create colors at any point in the visible spectrum (colors like teal, yellow, orange, etc.) by varying the geometry – primarily the diameter of the head – which would be useful for the application of full-color printing directly on c-Si wafers. Provided there can be good surface passivation [53], the nanopillar arrays could be utilized to achieve colors directly on the surface of c-Si solar cells either for light harvesting prints or for the creation of power-efficient reflective display devices which harvest light not used for coloration, an idea which has been explored in previous literature although to our knowledge not for c-Si [54–57].

4. Conclusion

In summary, we have demonstrated that arrays of hourglass-shaped Si nanopillars fabricated directly onto c-Si substrates can exhibit vibrant structural coloration. The hourglass shape acts to suspend the head of the pillars above the substrate such that they support strong Mie resonances allowing them to achieve a similar optical functionality to previously reported Mie resonator arrays on low index substrates. We have shown these structures experimentally and used an experimentally validated FDTD simulation model to elucidate the Mie resonance phenomena responsible for their optical behavior. We also investigated the angular dependence of the nanopillar arrays using COMSOL Multiphysics. Finally, we used a genetic algorithm with our FDTD model to optimize the geometry of the nanopillars to create the RGB primary colors corresponding to two different color spaces, sRGB and Adobe RGB. We believe that our results open interesting opportunities for the implementation of structural coloring in integrated semiconductor devices for various practical venues of interest.

Appendix A: Numerically simulated field plots and reflectance for the optimized Adobe RGB green structure

The electric and magnetic field plots for the optimized nanopillar geometry for the Adobe RGB green primary point and the corresponding floating head array are shown in Fig. 7. The field plots in Figs. 7(a) and 7(b) show that the nanopillar and the corresponding floating head array support nearly identical MD resonances. The reflectance curves shown in Fig. 7(c) are also nearly identical with the exception of some minor differences. This demonstrates that optimizing the neck of the nanopillars works to isolate the head resonance more effectively and produces a more pronounced resonance compared to the experimental results.

Optics EXPRESS

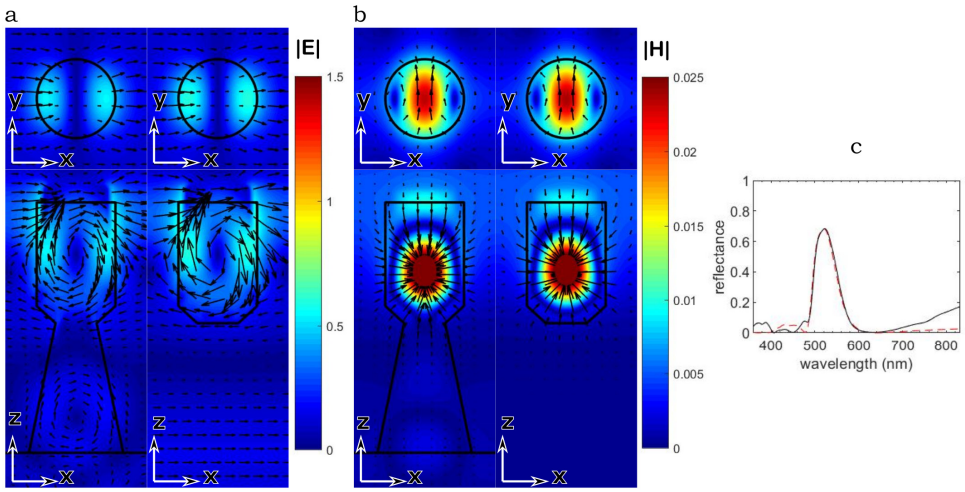

Fig. 7. (a) Electric field plots for the nanopillar array optimized for the Adobe RGB green primary point (left) and corresponding floating head array (right). (b) Magnetic field plots for the nanopillar array (left) and floating head array (right). (c) Reflectance of the two different structures (solid black is the nanopillar array and dashed red is the floating head array).

Appendix B: Extended analysis on the angle of incidence study

Here we provide further investigation for the dependence of the reflectance behavior on angle of incidence (AOI) that is seen in Fig. 5 from the main text. Field plots are provided at specific angles of incidence (AOI) in order to understand how the resonance of the nanopillars change as the AOI is increased. As discussed in the main text, the simulation is performed in COMSOL and is based on the green structure from the experimental results. The simulation is performed with TM (transverse magnetic) and TE (transverse electric) polarization and the power used to excite the structure is $P=|E|^2/2Z_0$ [W/m^2], where E=1[V/m].

Figure 8 shows magnetic and electric field plots excited with TM polarized illumination. Fig. 8(b) shows field plots when the illumination is at normal incidence. As discussed in the main text, the strong magnetic dipole (MD) resonance localized in the head of the green nanopillars occurs at the free space wavelength, λ=525 nm. As Fig. 5(c) in the main text shows, with TM polarized illumination the resonance peak moves to longer wavelengths as the AOI increases (λ=525 to λ=550 nm), and the reflectivity drops drastically due to a Brewster effect. Figure 8(c) confirms that at an AOI of θ=50° the magnetic and electric fields are no longer confined in the head but have leaked into the body of the nanopillars. This explains the reduced reflectance and also the shift to longer wavelengths since the resonance is distributed into the larger body of the pillar.

Optics EXPRESS

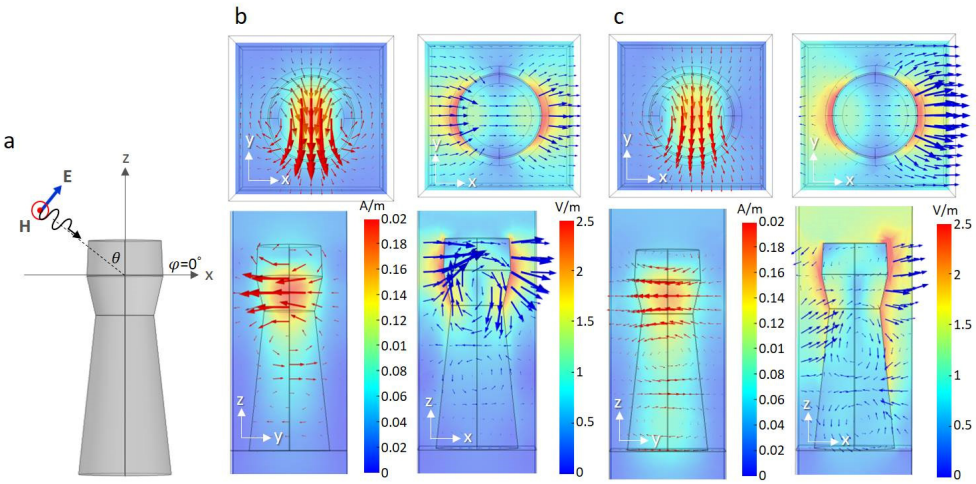

Fig. 8. (a) Schematic of the simulation with TM polarized illumination. (b) Magnetic (left) and electric (right) field plots of the nanopillar when θ = 0° and λ = 525 nm. (c) Magnetic (left) and electric (right) field plots of the nanopillar when θ = 50° and λ = 525 nm. Background color plots are absolute value of the field and arrows are field vectors.

As shown in Fig. 5(b) from the main text, for TE polarized illumination there is a broadening of the reflectance peak as the AOI increases. The broadening occurs due to the appearance of a new resonance which interacts with the full structure. This resonance happens at wavelengths shorter than the MD resonance and thus broadens the reflectance peak into the blue portion of the spectrum. This resonance is shown at θ=50° and λ=485 nm by the field plots in Fig. 9(b). The MD resonance from normal incidence generally maintains its position as the AOI increases as shown by the field plots at θ=50° and λ=525 nm in Fig. 9(c).

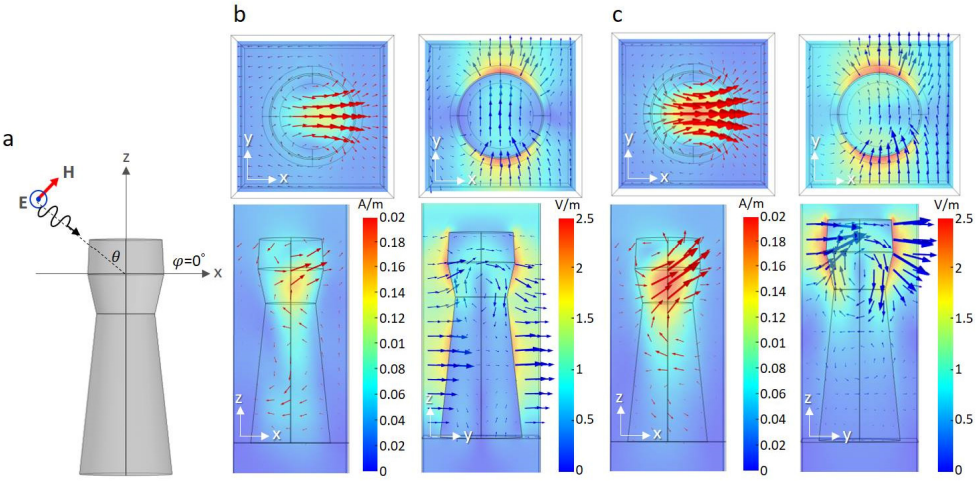

Fig. 9. (a) Schematic of the simulation with TE polarized illumination. (b) Magnetic (left) and electric (right) field plots of the nanopillar when θ = 50° and λ = 485 nm. (c) Magnetic (left) and electric (right) field plots of the nanopillar when θ = 50° and λ = 525 nm. Background color plots are absolute value of the field and arrows are field vectors.

Optics EXPRESS

Appendix C: Numerical simulations of RGB nanopillars with constant height

In order to investigate a potential monolithic fabrication scenario of red, green, and blue subpixels, we have run FDTD simulations to determine reflectance for a 3 different nanopillar arrays with constant height. These results are shown in Fig. 10. The red structure is taken directly from the results of the GA in section 3.4. The green and blue structures take their head dimensions and array pitch from the GA results, and then the parameter E is adjusted such that the total height is equal to the total height of the red structure. Thus, all 3 structures have the same height, as illustrated in Fig. 10(a). The results differ from the results of the optimization, especially in the green case, but generally maintain a wide color gamut. Note that the red result is identical since the same geometry is used in both cases.

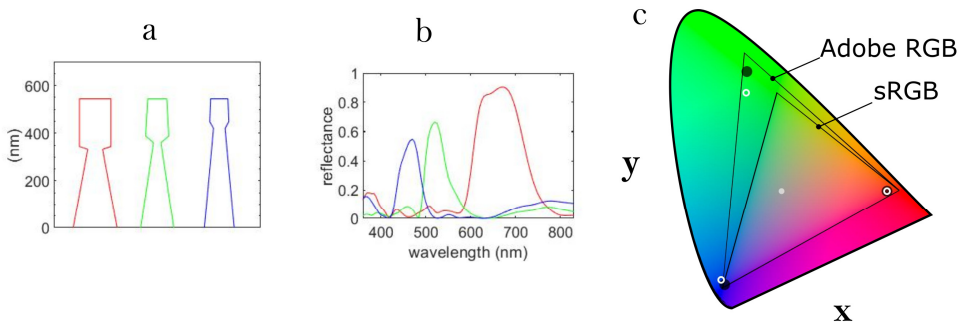

Fig. 10. (a) Plot showing the geometry of the three nanopillars (red, green, and blue left to right). (b) Simulated reflectance curves of the three structures. (c) CIE chromaticity plot with sRGB and Adobe RGB color spaces outlined by the black triangles, the D65 white point shown by the filled white circle in the middle, the three GA results shown by the black filled circles, and the three constant height results shown by the open white circles.

Appendix D: Photographs of fabricated 4" wafers

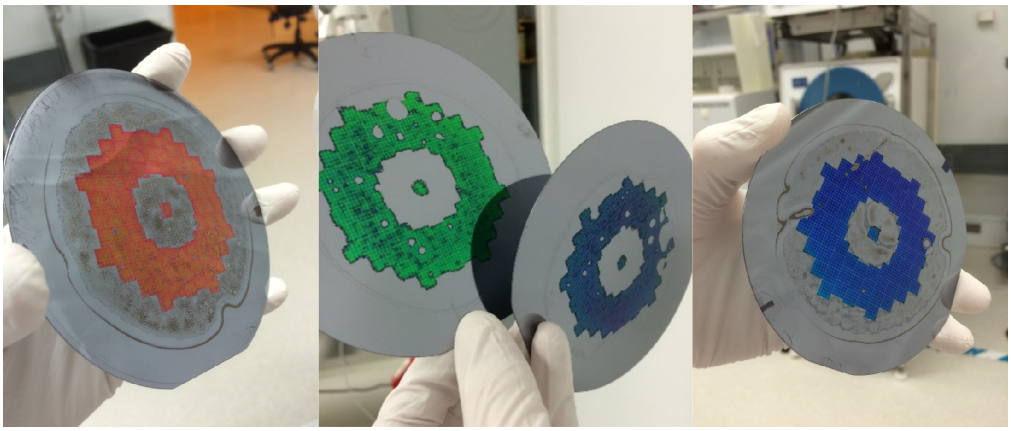

Fig. 11. Photographs of fabricated 4" wafers.

Funding

National Science Foundation (NSF) (EEC-1160494, ECCS-1542159); Scalable Nanomanufacturing Program (NSF) (ECCS-1120823).

Acknowledgments

This work was performed in part at the University of Texas Microelectronics Research Center, a member of the National Nanotechnology Coordinated Infrastructure (NNCI), which

Optics EXPRESS

is supported by the National Science Foundation. We would like to thank the T.W. Whaley, Jr. Friends of Alec Endowed Scholarship for funding Brian throughout multiple semesters. We would also like to thank Michelle Grigas for her expertise and gracious help in plasma etching.

Disclosures

The authors declare that there are no conflicts of interest related to this article.

References

1. J. V. Sanders, "Colour of precious opal," Nature **204**(4964), 1151–1153 (1964).
2. S. Kinoshita and S. Yoshioka, "Structural colors in nature: the role of regularity and irregularity in the structure," ChemPhysChem **6**(8), 1442–1459 (2005).
3. M. Srinivasarao, "Nano-optics in the biological world: beetles, butterflies, birds, and moths," Chem. Rev. **99**(7), 1935–1962 (1999).
4. P. Vukusic and J. R. Sambles, "Photonic structures in biology," Nature **424**(6950), 852–855 (2003).
5. Y. Zhao, Z. Xie, H. Gu, C. Zhu, and Z. Gu, "Bio-inspired variable structural color materials," Chem. Soc. Rev. **41**(8), 3297–3317 (2012).
6. J. Teyssier, S. V. Saenko, D. van der Marel, and M. C. Milinkovitch, "Photonic crystals cause active colour change in chameleons," Nat. Commun. **6**(1), 6368 (2015).
7. C. Ji, K.-T. Lee, T. Xu, J. Zhou, H. J. Park, and L. J. Guo, "Engineering light at the nanoscale: structural color filters and broadband perfect absorbers," Adv. Opt. Mater. **5**(20), 1700368 (2017).
8. M. Decker and I. Staude, "Resonant dielectric nanostructures: a low-loss platform for functional nanophotonics," J. Opt. **18**(10), 103001 (2016).
9. A. Kristensen, J. K. W. Yang, S. I. Bozhevolnyi, S. Link, P. Nordlander, N. J. Halas, and N. A. Mortensen, "Plasmonic colour generation," Nat. Rev. Mater. **2**(1), 16088 (2017).
10. Y. Gu, L. Zhang, J. K. Yang, S. P. Yeo, and C.-W. Qiu, "Color generation via subwavelength plasmonic nanostructures," Nanoscale **7**(15), 6409–6419 (2015).
11. K. Kumar, H. Duan, R. S. Hegde, S. C. W. Koh, J. N. Wei, and J. K. W. Yang, "Printing colour at the optical diffraction limit," Nat. Nanotechnol. **7**(9), 557–561 (2012).
12. X. M. Goh, Y. Zheng, S. J. Tan, L. Zhang, K. Kumar, C.-W. Qiu, and J. K. W. Yang, "Three-dimensional plasmonic stereoscopic prints in full colour," Nat. Commun. **5**(1), 5361 (2014).
13. S. J. Tan, L. Zhang, D. Zhu, X. M. Goh, Y. M. Wang, K. Kumar, C.-W. Qiu, and J. K. W. Yang, "Plasmonic color palettes for photorealistic printing with aluminum nanostructures," Nano Lett. **14**(7), 4023–4029 (2014).
14. P. R. West, S. Ishii, G. V. Naik, N. K. Emani, V. M. Shalaev, and A. Boltasseva, "Searching for better plasmonic materials," Laser Photonics Rev. **4**(6), 795–808 (2010).
15. Y. Kanamori, M. Shimono, and K. Hane, "Fabrication of transmission color filters using silicon subwavelength gratings on quartz substrates," IEEE Photonics Technol. Lett. **18**(20), 2126–2128 (2006).
16. M. J. Uddin and R. Magnusson, "Highly efficient color filter array using resonant Si3N4 gratings," Opt. Express **21**(10), 12495–12506 (2013).
17. Y.-T. Yoon, H.-S. Lee, S.-S. Lee, S. H. Kim, J.-D. Park, and K.-D. Lee, "Color filter incorporating a subwavelength patterned grating in poly silicon," Opt. Express **16**(4), 2374–2380 (2008).
18. M. Khorasaninejad, N. Abedzadeh, J. Walia, S. Patchett, and S. S. Saini, "Color matrix refractive index sensors using coupled vertical silicon nanowire arrays," Nano Lett. **12**(8), 4228–4234 (2012).
19. H. Park, Y. Dan, K. Seo, Y. J. Yu, P. K. Duane, M. Wober, and K. B. Crozier, "Filter-free image sensor pixels comprising silicon nanowires with selective color absorption," Nano Lett. **14**(4), 1804–1809 (2014).
20. K. Seo, M. Wober, P. Steinvurzel, E. Schonbrun, Y. Dan, T. Ellenbogen, and K. B. Crozier, "Multicolored vertical silicon nanowires," Nano Lett. **11**(4), 1851–1856 (2011).
21. Z. Yang, Y. Chen, Y. Zhou, Y. Wang, P. Dai, X. Zhu, and H. Duan, "Microscopic Interference Full-Color Printing Using Grayscale-Patterned Fabry–Perot Resonance Cavities," Adv. Opt. Mater. **5**(10), 1700029 (2017).
22. Y. Yang, Y. Zhou, Y. Chen, Y. Wang, P. Dai, Z. Zhang, and H. Duan, "Reflective color filters and monolithic color printing based on asymmetric Fabry–Perot cavities using nickel as a broadband absorber," Adv. Opt. Mater. **4**(8), 1196–1202 (2016).
23. J. Hong, E. Chan, T. Chang, T.-C. Fung, B. Hong, C. Kim, J. Ma, Y. Pan, R. Van Lier, S. Wang, B. Wen, and L. Zhou, "Continuous color reflective displays using interferometric absorption," Optica **2**(7), 589–597 (2015).
24. A. C. Arsenault, D. P. Puzzo, I. Manners, and G. A. Ozin, "Photonic-crystal full-colour displays," Nat. Photonics **1**(8), 468–472 (2007).
25. P. Kang, S. O. Ogunbo, and D. Erickson, "High resolution reversible color images on photonic crystal substrates," Langmuir **27**(16), 9676–9680 (2011).
26. H. S. Lee, T. S. Shim, H. Hwang, S.-M. Yang, and S.-H. Kim, "Colloidal photonic crystals toward structural color palettes for security materials," Chem. Mater. **25**(13), 2684–2690 (2013).
27. G. Brönstrup, N. Jahr, C. Leiterer, A. Csáki, W. Fritzsche, and S. Christiansen, "Optical properties of individual silicon nanowires for photonic devices," ACS Nano **4**(12), 7113–7122 (2010).

Optics EXPRESS

28. L. Cao, P. Fan, E. S. Barnard, A. M. Brown, and M. L. Brongersma, "Tuning the color of silicon nanostructures," Nano Lett. **10**(7), 2649–2654 (2010).
29. A. I. Kuznetsov, A. E. Miroshnichenko, M. L. Brongersma, Y. S. Kivshar, and B. Luk'yanchuk, "Optically resonant dielectric nanostructures," Science **354**(6314), aag2472 (2016).
30. I. Staude, A. E. Miroshnichenko, M. Decker, N. T. Fofang, S. Liu, E. Gonzales, J. Dominguez, T. S. Luk, D. N. Neshev, I. Brener, and Y. Kivshar, "Tailoring directional scattering through magnetic and electric resonances in subwavelength silicon nanodisks," ACS Nano **7**(9), 7824–7832 (2013).
31. G. Mie, Albuquerque, New Mexico SAND78-. National Translation Center, Chicago, ILL, Translation, "Contributions on the optics of turbid media, particularly of colloidal metal solutions," 79–21946.
32. V. Flauraud, M. Reyes, R. Paniagua-Dominguez, A. I. Kuznetsov, and J. Brugger, "Silicon nanostructures for bright field full color prints," ACS Photonics **4**(8), 1913–1919 (2017).
33. E. Højlund-Nielsen, J. Weirich, J. Nørregaard, J. Garnaes, N. A. Mortensen, and A. Kristensen, "Angle-independent structural colors of silicon," J. Nanophotonics **8**(1), 083988 (2014).
34. Y. Kanamori, T. Ozaki, and K. Hane, "Reflection color filters of the three primary colors with wide viewing angles using common-thickness silicon subwavelength gratings," Opt. Express **22**(21), 25663–25672 (2014).
35. Y. Nagasaki, M. Suzuki, I. Hotta, and J. Takahara, "Control of Si-based all-dielectric printing color through oxidation," ACS Photonics **5**(4), 1460–1466 (2018).
36. Y. Nagasaki, M. Suzuki, and J. Takahara, "All-dielectric dual-color pixel with subwavelength resolution," Nano Lett. **17**(12), 7500–7506 (2017).
37. C.-S. Park, V. R. Shrestha, W. Yue, S. Gao, S.-S. Lee, E.-S. Kim, and D.-Y. Choi, "Structural color filters enabled by a dielectric metasurface incorporating hydrogenated amorphous silicon nanodisks," Sci. Rep. **7**(1), 2556 (2017).
38. J. Proust, F. Bedu, B. Gallas, I. Ozerov, and N. Bonod, "All-dielectric colored metasurfaces with silicon Mie resonators," ACS Nano **10**(8), 7761–7767 (2016).
39. S. Sun, Z. Zhou, C. Zhang, Y. Gao, Z. Duan, S. Xiao, and Q. Song, "All-dielectric full-color printing with TiO2 metasurfaces," ACS Nano **11**(5), 4445–4452 (2017).
40. V. Vashistha, G. Vaidya, R. S. Hegde, A. E. Serebryannikov, N. Bonod, and M. Krawczyk, "All-dielectric metasurfaces based on cross-shaped resonators for color pixels with extended gamut," ACS Photonics **4**(5), 1076–1082 (2017).
41. T. Wood, M. Naffouti, J. Berthelot, T. David, J.-B. Claude, L. Métayer, A. Delobbe, L. Favre, A. Ronda, I. Berbezier, N. Bonod, and M. Abbarchi, "All-dielectric color filters using SiGe-based Mie resonator arrays," ACS Photonics **4**(4), 873–883 (2017).
42. I. Koirala, S.-S. Lee, and D.-Y. Choi, "Highly transmissive subtractive color filters based on an all-dielectric metasurface incorporating TiO_2 nanopillars," Opt. Express **26**(14), 18320–18330 (2018).
43. E.-H. Cho, H.-S. Kim, B.-H. Cheong, O. Prudnikov, W. Xianyua, J.-S. Sohn, D.-J. Ma, H.-Y. Choi, N.-C. Park, and Y.-P. Park, "Two-dimensional photonic crystal color filter development," Opt. Express **17**(10), 8621–8629 (2009).
44. Z. Dong, J. Ho, Y. F. Yu, Y. H. Fu, R. Paniagua-Dominguez, S. Wang, A. I. Kuznetsov, and J. K. W. Yang, "Printing beyond sRGB color gamut by mimicking silicon nanostructures in free-space," Nano Lett. **17**(12), 7620–7628 (2017).
45. M. Garín, M. Solà, A. Julian, and P. Ortega, "Enabling silicon-on-silicon photonics with pedestalled Mie resonators," Nanoscale **10**(30), 14406–14413 (2018).
46. D. Franklin, R. Frank, S.-T. Wu, and D. Chanda, "Actively addressed single pixel full-colour plasmonic display," Nat. Commun. **8**, 15209 (2017).
47. H. Liu, Y. Yao, Y. Wang, and W. Wu, "Full-color reflective display system based on high contrast gratings," J. Vac. Sci. Technol. B **32**(6), 06FE04 (2014).
48. Y. Gao, C. Huang, C. Hao, S. Sun, L. Zhang, C. Zhang, Z. Duan, K. Wang, Z. Jin, N. Zhang, A. V. Kildishev, C.-W. Qiu, Q. Song, and S. Xiao, "Lead Halide Perovskite nanostructures for dynamic color display," ACS Nano **12**(9), 8847–8854 (2018).
49. Y.-F. Huang, S. Chattopadhyay, Y.-J. Jen, C.-Y. Peng, T.-A. Liu, Y.-K. Hsu, C.-L. Pan, H.-C. Lo, C.-H. Hsu, Y.-H. Chang, C.-S. Lee, K.-H. Chen, and L.-C. Chen, "Improved broadband and quasi-omnidirectional anti-reflection properties with biomimetic silicon nanostructures," Nat. Nanotechnol. **2**(12), 770–774 (2007).
50. X. Li, P. C. Li, L. Ji, C. Stender, C. McPheeters, S. R. Tatavarti, K. Sablon, and E. T. Yu, "Subwavelength nanostructures integrated with polymer-packaged iii–v solar cells for omnidirectional, broad-spectrum improvement of photovoltaic performance," Prog. Photovolt. Res. Appl. **23**(10), 1398–1405 (2015).
51. A. Rahman, A. Ashraf, H. Xin, X. Tong, P. Sutter, M. D. Eisaman, and C. T. Black, "Sub-50-nm self-assembled nanotextures for enhanced broadband antireflection in silicon solar cells," Nat. Commun. **6**(1), 5963 (2015).
52. A. Alù, G. D'Aguanno, N. Mattiucci, and M. J. Bloemer, "Plasmonic Brewster angle: broadband extraordinary transmission through optical gratings," Phys. Rev. Lett. **106**(12), 123902 (2011).
53. W.-C. Wang, C.-W. Lin, H.-J. Chen, C.-W. Chang, J.-J. Huang, M.-J. Yang, B. Tjahjono, J.-J. Huang, W.-C. Hsu, and M.-J. Chen, "Surface passivation of efficient nanotextured black silicon solar cells using thermal atomic layer deposition," ACS Appl. Mater. Interfaces **5**(19), 9752–9759 (2013).
54. J. Y. Lee, K.-T. Lee, S. Seo, and L. J. Guo, "Decorative power generating panels creating angle insensitive transmissive colors," Sci. Rep. **4**(1), 4192 (2015).

Optics EXPRESS

55. K.-T. Lee, J. Y. Lee, T. Xu, H. J. Park, and L. J. Guo, "Colored dual-functional photovoltaic cells," J. Opt. **18**(6), 064003 (2016).
56. H. J. Park, T. Xu, J. Y. Lee, A. Ledbetter, and L. J. Guo, "Photonic color filters integrated with organic solar cells for energy harvesting," ACS Nano **5**(9), 7055–7060 (2011).
57. L. Wen, Q. Chen, S. Song, Y. Yu, L. Jin, and X. Hu, "Photon harvesting, coloring and polarizing in photovoltaic cell integrated color filters: efficient energy routing strategies for power-saving displays," Nanotechnology **26**(26), 265203 (2015).